POLITECNICO DI TORINO
Repository ISTITUZIONALE

Optimization of CaCO3 synthesis through the carbonation route in a packed bed reactor

Original
Optimization of CaCO3 synthesis through the carbonation route in a packed bed reactor / Liendo, F., Arduino, M., Deorsola, F.A., Bensaid, S.. - In: POWDER TECHNOLOGY. - ISSN 0032-5910. - ELETTRONICO. - 377:(2021), pp. 868-881. [10.1016/j.powtec.2020.09.036]

Availability:
This version is available at: 11583/2846652 since: 2020-09-24T14:05:11Z

Publisher:
Elsevier

Published
DOI:10.1016/j.powtec.2020.09.036

Terms of use:

This article is made available under terms and conditions as specified in the corresponding bibliographic description in the repository

Publisher copyright

(Article begins on next page)

25 November 2026

Powder Technology 377 (2021) 868–881

Contents lists available at ScienceDirect

Powder Technology

journal homepage: www.elsevier.com/locate/powtec

Optimization of $CaCO_3$ synthesis through the carbonation route in a packed bed reactor

Freddy Liendo, Mara Arduino, Fabio A. Deorsola *, Samir Bensaid

Department of Applied Science and Technology, Politecnico di Torino, Corso Duca degli Abruzzi, 24, 10129 Torino, Italy

ARTICLE INFO

Article history:
Received 9 January 2020
Received in revised form 9 July 2020
Accepted 18 September 2020
Available online 22 September 2020

Keywords:
Precipitation
Calcite
Reactive absorption
Nanoparticles
Particle morphology

ABSTRACT

This article presents an investigation on the recovery of CO_2 from the combustion gases of the cement industry through a carbonation route in order to obtain Calcium Carbonate Nanoparticles (CCnP), which could find application as either polymer or cement fillers. Two different experimental setups, a Continuously Stirred Bubbling Reactor (CSBR) and a Packed Bed Reactor (PBR), were studied in order to improve the final product and enhance the process yield. The influence of the experimental parameters on the particle size and morphology was tested for both reactors. The process was intensified by employing the PBR, where cubic calcite particles smaller than 300 nm were synthesized and higher CO_2 conversions were obtained with respect to the CSBR performance.
© 2020 The Authors. Published by Elsevier B.V. This is an open access article under the CC BY-NC-ND license (http://creativecommons.org/licenses/by-nc-nd/4.0/).

1. Introduction

Nowadays, there are serious environmental issues around global warming, principally due to the Greenhouse Gas (GHG) emissions, mainly carbon dioxide CO_2. Several industries characterized by a high energy intensity processes are responsible for the emission of these gases; these include the cement, iron, steel, chemical, pulp and paper, aluminium and other industries. The cement industry is reported to produce about 8% of global emissions of CO_2 [1]. The carbon footprint of this industry is equal to 680 kg CO_2 equivalent per cement ton. Several CO_2 capture, reuse and storage technologies have been developed, which involve physical, chemical and even biological processes. Absorption processes are the most widely used in commercial applications although several CO_2 capture techniques such as adsorption, membrane and cryogenic methods have been developed [2]. Despite the technology readiness of the different CO_2 capture technologies, a primary challenge is the need for reuse alternatives for the available CO_2, which must prove to be cost-effective and to lead to a net sequestration of CO_2 as compared to the current scenario. Even more attractive is the possibility to generate products that add competitiveness to the sectors that are nowadays the major CO_2 emitters, at the same time lowering their GHG footprint.

For these reasons, the achievement of an added value product obtained from the recovery of CO_2 from combustion gases of the cement industry was investigated as the objective of this study. The synthesis of Calcium Carbonate Nanoparticles (CCnP), with the final purpose of incorporating them within the cement as an additive, could reach the target of capturing and sequestrating CO_2 as well as leading to a product with equivalent or even superior properties, which would increase its market value.

CCnP have been widely synthesized via the carbonation route [3–7]. Ramakrishna et al. produced microsized $CaCO_3$ particles starting from a $Ca(OH)_2$ slurry solution via the carbonation route. Ulkeryildiz et al. produced hollow nano calcite starting from a $Ca(OH)_2$ slurry, by employing a jet flow reactor where the precipitation zone was separated from the stabilitation zone in order to avoid agglomeration and growth phenomenas. Instead, Ryu et al. synthesized microsized $CaCO_3$ particles starting from NH_4OH. Starting from a $CaCl_2$ solution, Sun and coworkers synthesized CCnP by employing an innovative rotating packed bed, where a simultaneous absorption of CO_2 and NH_3 absorption occurred.

In general, this approach involves a precipitation phenomenon driven by a reaction, where there is an interaction between the precipitation and the mass transfer process, given the multiphase nature of the process. The mass transfer has a very important effect on the precipitation process, since simultaneous crystal formation may occur in the bulk solution as well as in a thin interfacial region, according to the gas absorption rate. Actually, the precipitation can take place in both zones, and then the two zones can interact with each other, under the action of the fluid in which they are contained. The nucleation and growth are influenced by the saturation level determined by Eq. 1, where $a_{Ca^{2+}}$, $a_{CO3^{2-}}$ and k_{sp} are the activity coefficient of calcium ions, carbonate ions and the solubility product of the $CaCO_3$, respectively.

* Corresponding author.
E-mail address: fabio.deorsola@polito.it (F.A. Deorsola).

https://doi.org/10.1016/j.powtec.2020.09.036
0032-5910/© 2020 The Authors. Published by Elsevier B.V. This is an open access article under the CC BY-NC-ND license (http://creativecommons.org/licenses/by-nc-nd/4.0/).

$$S = \sqrt{\left(a_{Ca^{2+}} * a_{CO_3^{2-}}\right)/k_{sp}} \quad (1)$$

Precipitated calcium carbonate has received much attention owing to its wide application in such industrial fields as paper, rubber, plastics, paint, etc. [8]. Currently, it is widely used as cement filler in order to decrease production costs and to improve some of the mechanical properties of the composite materials [9,10]. However, unlike from some attempts in the literature and in already established industrial practices, the current work focuses on obtaining CCnP, characterized by a nanosized distribution that (with other filling materials) was demonstrated to be beneficial for the enhancement of cement mechanical properties [11,12].

Moreover, the CO_2 reused for the production of $CaCO_3$ via carbonation of a calcium solution in alkaline conditions produces CCnP which can be used as filler in the cement; this can contribute to a CO_2 circular economy as indicated in Fig. 1.

Many industrial wastes like wollastonite [13] and steelmaking slag contain high amounts of CaO, which can be exploited for $CaCO_3$ synthesis. In fact, the extraction and reutilization of the CO_2 has been previously studied [14,15]. Ragipani and co-workers carried out a precipitation of $CaCO_3$ via a CO_2 pressure-swing technique reaching high yields of the overall recovery or Ca^{2+} as $CaCO_3$ [14]. Instead, Tinchana et al. studied the leaching of steelmaking with acetic acid and deionized water and concluded that the deionized water leaching process is adequate for steelmaking slag extraction for CO_2 sequestration [15].

Therefore, in this work a carbonation process of a CaO slurry as a synthesis route to produce calcium carbonate nanoparticles was studied and enhanced through two kinds of reactors. The aim of this research was double: from one hand, to demonstrate the influence of the mixing efficiency on the dimension and size distribution of the $CaCO_3$ particles; on the other one, to provide a novel and simple precipitation setup characterized by ease of scale up, low energy consumption, atmospheric operating pressure and versatility in the control and customization of the particles size for a wide range of final applications.

Table 1
Properties of the anhydrous crystalline phases [11,12] [16–18].

Phase	Crystallographic unit cell	Specific Gravity	Toughness
Calcite	Hexagonal (rhombohedral)	2.71 g/cm^3	Brittle
Vaterite	Hexagonal	2.65 g/cm^3	Brittle
Aragonite	Orthorhombic	2.93 g/cm^3	Brittle

1.1. $CaCO_3$ precipitation mechanism

Since calcium carbonate is sparingly soluble and its K_{ps} is equal to $4.4 \cdot 10^{-9}$, it is easily synthesized by a precipitation method. Different calcium carbonate polymorphs can be obtained according to the operating conditions. Calcite is the most stable calcium carbonate phase, while aragonite and vaterite are metastable and instable phases [16]. At higher temperatures, aragonite becomes more stable than the other calcium carbonate polymorphs [17,18]. Table 1 summarizes some properties of the anhydrous crystalline phases.

$CaCO_3$ particle formation can follow the pathway hereafter described. In a saturated solution of Ca^{2+} and CO_3^{2-} ions (Eq. 2), the precipitation reaction takes place: calcium cations bond with carbonate ions forming calcium carbonate embryos in solution. The embryos then grow to form a critical nucleus, which, if local conditions are favourable, grows to form a primary nanoparticle [5]. As shown, three stages can be individuated in normal conditions (Fig. 2). In the first stage, a prevalence of amorphous calcium carbonate can be observed. In the second stage, a coexistence of vaterite and calcite is present, while in the third and final stage calcite is practically the only phase present [19].

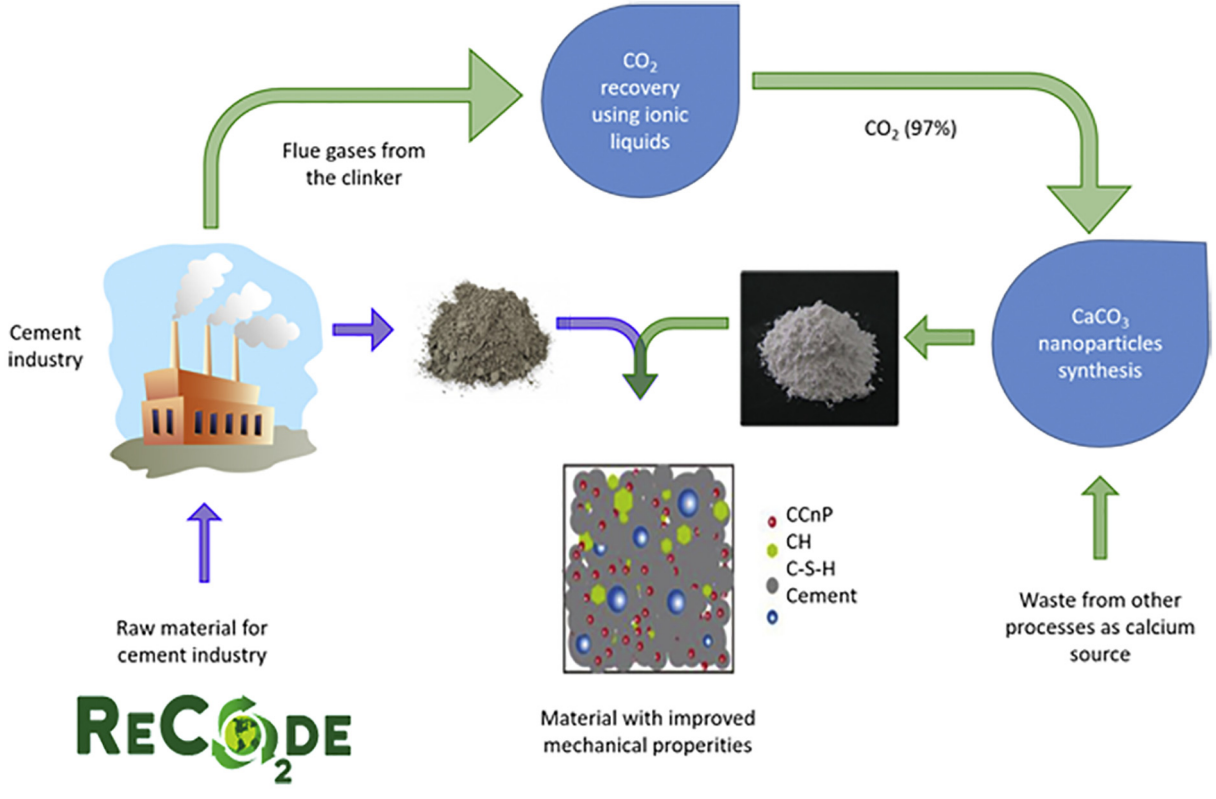


Fig. 1. Circular economy process scheme of CO_2 reuse in the cement industry (process designed within the RECODE project -see acknowledgments).

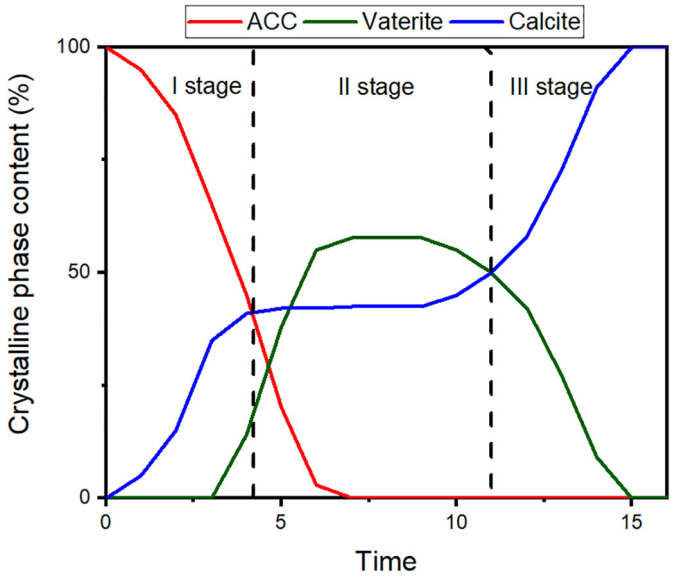


Fig. 2. Change in the polymorphic abundance of $CaCO_3$.

$$Ca^{2+}_{(aq)} + CO^{2-}_{3(aq)} \leftrightarrow CaCO_{3(s)}\downarrow \quad (2)$$

At the top left of Fig. 3, the precipitation diagram of different calcium carbonate polymorph is shown [20]. As reported previously, calcite is the most stable polymorph at any temperature, since it has the lowest solubility of calcium carbonate phases, due to its lower Activity Product (AP). So, hypothesizing a precipitation process of calcium carbonate, at the beginning of the process, with a high concentration of Ca^{2+} and CO_3^{2-} ions, supersaturation conditions for every phase are realized. The driving force for nucleation is given by Eq. 3. In the first stage of the calcium carbonate precipitation process, Amorphous Calcium Carbonate (ACC) is present in a great percentage. In the second stage, when the concentration gets lower, no more supersaturation conditions of ACC are present, and it gets dissolved again; because of this, in the second stage calcite and vaterite are present contemporaneously. At the end of the process, at lower concentrations, vaterite is no longer saturated and it dissolves in solution again, with only calcite present at the end of the process [19,21].

The transformation mechanism from ACC to the anhydrous crystalline polymorph can be related to the chemical composition of the local environment [19,22]. That is, the synthesis method has an important role in the final properties of the calcium carbonate particles; principally, the operational parameters of the CO_2 bubbling lead to the synthesis of particles with different shapes and sizes, but poor control of the particle size distribution. Instead, through biomimetic methods and the use of suitable additives better control of the particles properties can be achieved [23].

$$\frac{\Delta\mu_i}{K_B T} = Ln\,AP - Ln\,K_i \quad (3)$$

where:

$\Delta\mu_i$ = Chemical Potential.

K_B = Boltzmann Constant

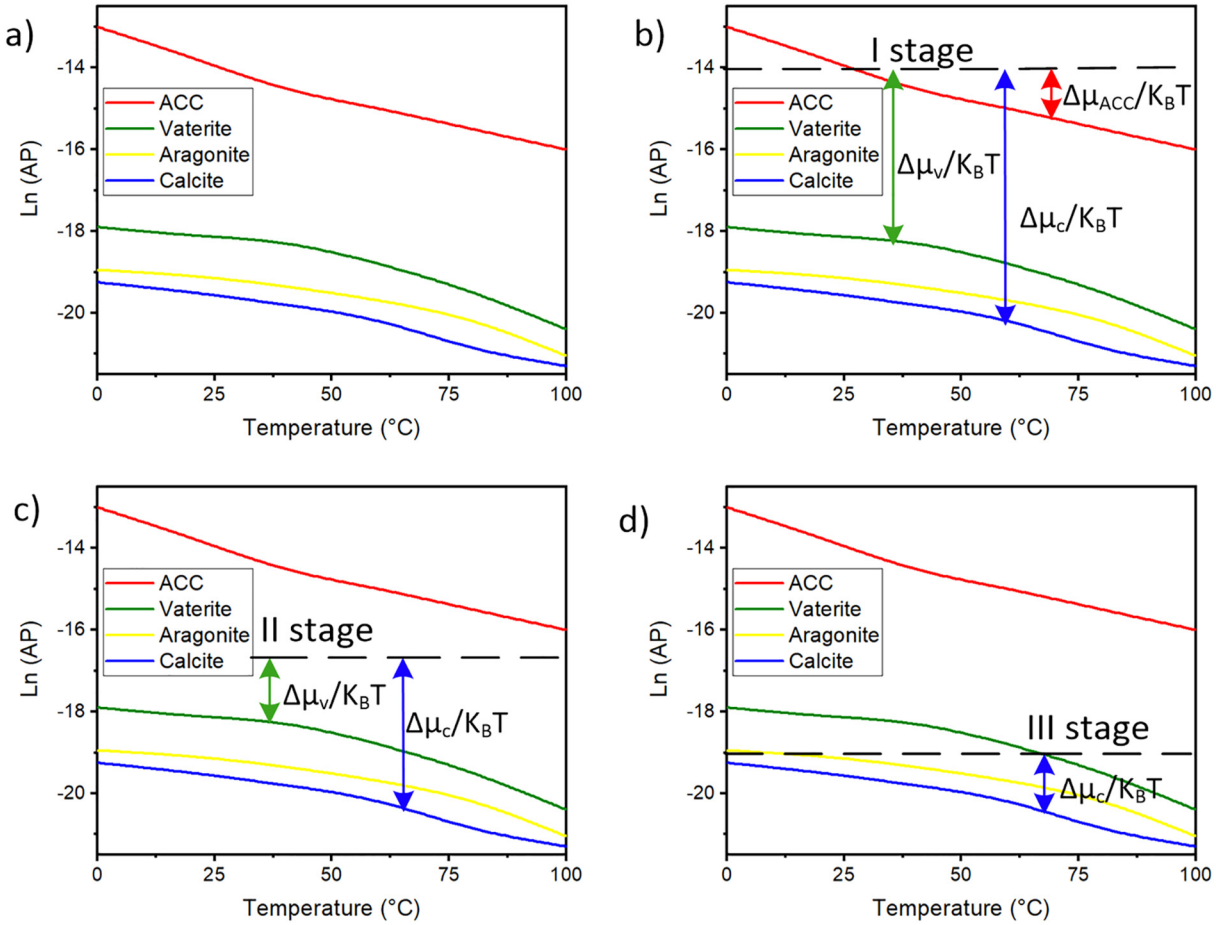


Fig. 3. Calcium carbonate precipitation diagram [20]. a) Precipitation diagram b) I stage of the precipitation process, c) II stage, d) III stage.

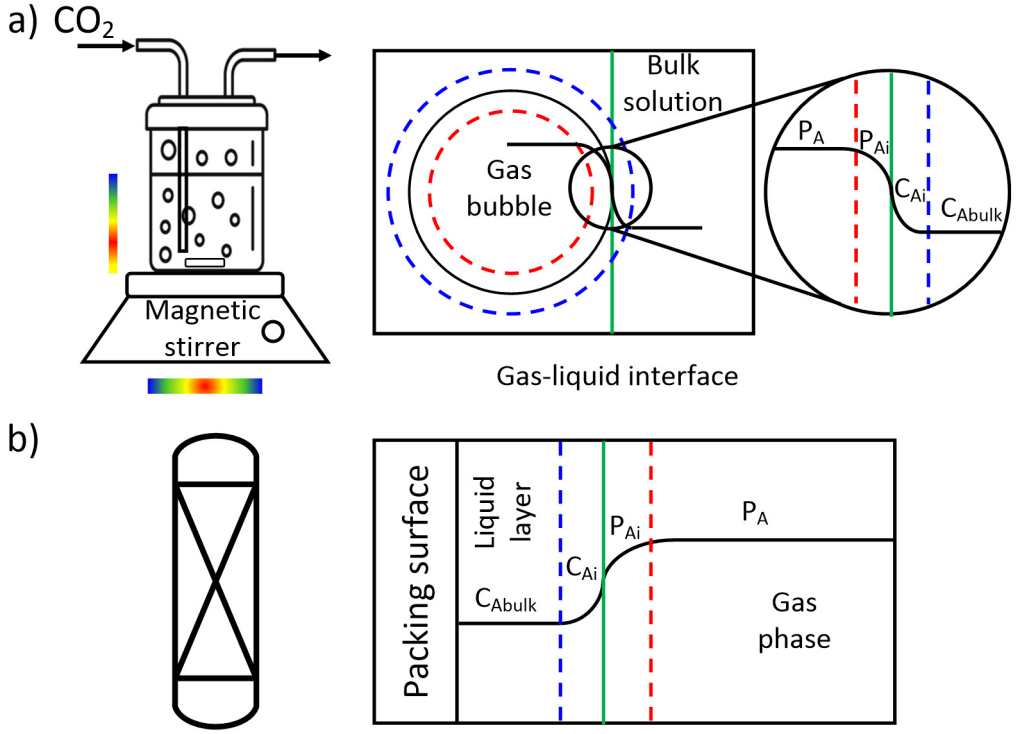


Fig. 4. CO_2 absorption mechanism in both cases. a) Bubbling reactor. b) Packed bed reactor.

T = Temperature

K_i = Activity product of the saturated state.

Chemical reaction, nucleation and growth are the three main steps. In reality, they do not occur in this specific order but simultaneously, therefore it is worth controlling these three steps during precipitation. High degrees of supersaturation lead to the nucleation of small particles. By achieving high degrees of $CaCO_3$ supersaturation, uniform spatial concentration distributions and identical growth time for all crystals, nano-$CaCO_3$ with narrow size distribution can be obtained. Macromixing and micromixing occur simultaneously in the reactors. Uniform spatial concentration distribution of any component on the vessel scale can only be achieved by macromixing, while uniform spatial concentration distribution on the molecular scale can be reached by intense micromixing [24]. Hence, the CO_2 absorption mechanism takes a

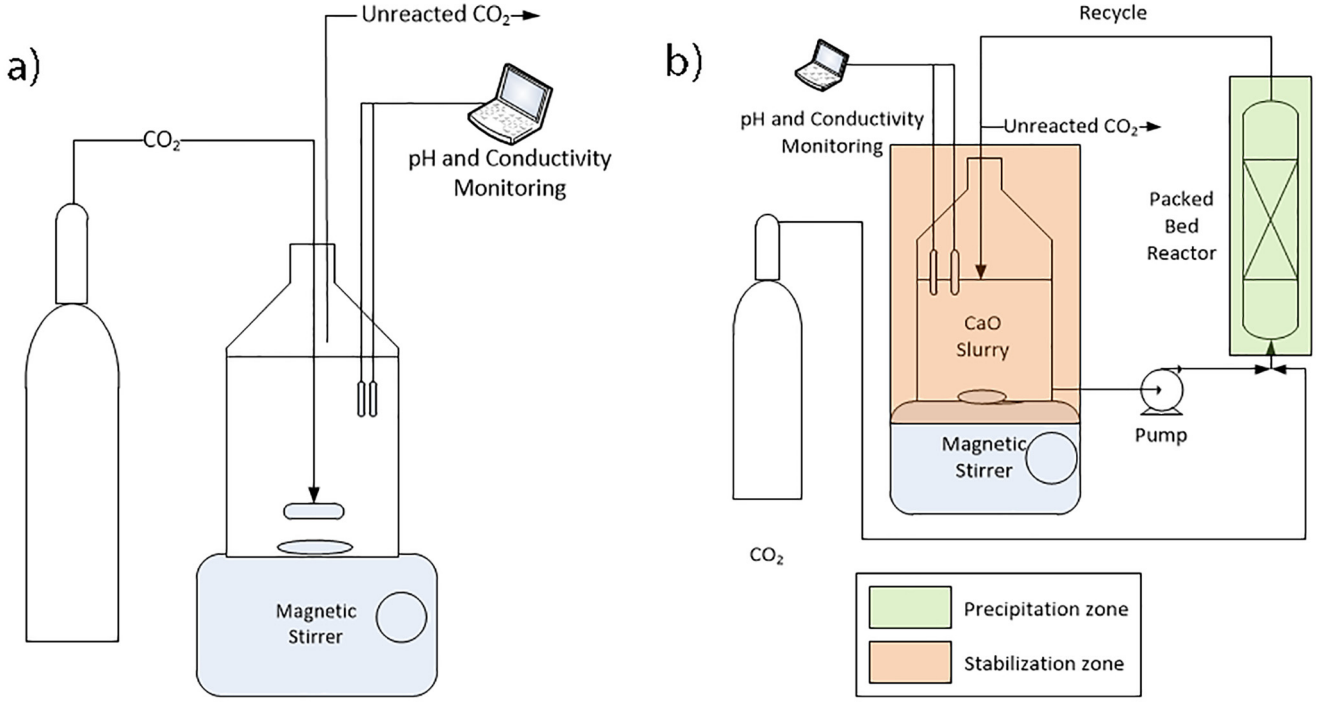


Fig. 5. Different experimental setup employed. a) Bubbling reactor b) Packed bed reactor.

Table 2
Packed bed reactor parameters.

System Parameters	
Length (mm)	370
Inner Diameter (mm)	10
Packing Surface Area (m^2/m^3)	1200
ε (m^3/m^3)	0.62

crucial role in the $CaCO_3$ particles synthesis in order to obtain a high micromixing level. Micromixing is a key factor determining the degree of the supersaturation concentration of the solute and its local spatial distribution [4].

1.2. CO_2 absorption mechanism

Considering the use of pure CO_2 (99.99%), the main resistance of the mass transfer is given by the liquid phase, thus it controls the absorption process [25]. The liquid film is affected by different factors. In this case, a reactive absorption of CO_2 is considered, since it reacts with the OH^- ions according to the Eq. 4 and Eq. 5. The rate of carbon dioxide absorption is considerably enhanced due to this fast reaction [25]. In this work, the effect of the effectiveness of the absorption process on calcium carbonate precipitation was studied.

$$CO_2 + OH^- \leftrightarrow HCO_3^- \quad (4)$$

$$HCO_3^- + OH^- \leftrightarrow CO_3^{2-} \quad (5)$$

In a continuously stirred bubbling reactor (CSBR), illustrated in Fig. 4a, the gas stream is fed to the reactor through the sparger at the bottom of the reactor, forming small or big bubbles according to the process conditions. The area of these bubbles therefore influences the mass transfer rate. Furthermore, in a BR, there are many segregation problems, therefore, the supersaturation grade would not be homogeneous in the whole reactor, as illustrated in Fig. 4a. Consequently, carrying out the precipitation process in a conventional apparatus, such as a stirred tank reactor, entails issues in controlling the quality of the product and the morphology as well as the size distribution of the particles often change from one batch to another [4,26]. This is caused by the poor micromixing present in these kinds of reactor [4].

By employing a Packed Bed Reactor (PBR) in the experiment, this issue was reduced and the micromixing was enhanced by optimizing the operating conditions. In this kind of reactor, the liquid forms a layer over the packing, which has a thickness (δ) that depends on the flow regime of the process, as seen in Fig. 4b. The flow regime has an important influence on the mass transfer coefficient. Film thickness plays a fundamental role: a thin film and sufficient turbulent conditions provide a uniform concentration on the vessel scale and molecular scale, by intense macro and micromixing, respectively, which result in an enhanced CO_2 mass transfer and great increase of the nucleation rate [4].

Table 3
Run parameters of CSBR tests.

Run	Initial CaO concentration (mol/L)	Gas flowrate (mL/min)	Gas residence time (s)[a]
1	0.015	100	0.38
2	0.015	225	0.27
3	0.015	571	0.19
4	0.015	1450	0.13
5	0.025	225	0.27
6	0.05	225	0.27

[a] calculated by estimating the velocity of a singular bubble with the dimensions equal to which generated at the sparger, for the different operating conditions.

Table 4
Run parameters of PBR tests.

Run	Initial CaO concentration (mol/L)	Gas flowrate (mL/min)	Gas residence time (min)[a]	Liquid Flowrate (mL/min)	Liquid residence time (min)[a]
7	0.015	100	0.291	108	0.269
8	0.015	225	0.129	108	0.269
9	0.015	571	0.051	108	0.269
10	0.015	1450	0.020	108	0.269
11	0.015	1450	0.020	250	0.116
12	0.015	1450	0.020	350	0.083
13	0.015	1450	0.020	400	0.073
14	0.025	225	0.129	108	0.269
15	0.05	225	0.129	108	0.269

[a] calculated by the ratio between the flowrate and the volume of the PBR free of packaging, without considering the presence of the liquid reducing the space for the gas to pass through the column, and vice versa.

By controlling these factors, small particles with a narrow particles size distribution were expected. The liquid flow effect on the film thickness has been widely studied [27–29]. Researchers performed the visual study of liquid flow in the PBR and established a model to represent the flow patterns, which indicated that the liquid in the packing existed as films attached to the packing wire and filling the voids of the packing. Zhao et al. concluded that three parameters should be correlated to the experimental data: the relative thickness of the liquid (δ), the viscous effects (Re, Reynolds number) and the capillary effects (Ca, Capillary number) [29]. In addition, the study of the flow regime in concurrent gas-liquids upward flow through a packed bed was performed by Murugesan et al. [30], who concluded that flow regime transitions and the frictional pressure drop are strongly influenced by all the fundamental variables as well as the operating variables of the system considered [30]. They developed a correlation for the estimation, according to the operating conditions, of the three different flow regimes in packed beds (bubble, dispersed bubble and pulse) which are considered in this work. These three different regimes have an influence on the mass transfer surface area and micromixing; hence, by controlling this, the absorption-precipitation process can be enhanced.

In the boundary phase region, different mechanisms take place after the carbon dioxide absorption, which are considerably enhanced due to the fast reaction between carbon dioxide and hydroxyl ions (see Eq. 4). This reaction, at the same time, is boosted by the subsequent reaction between bicarbonate ions and hydroxyl ones for the carbonate ions formation according to Eq. 5. Then, the presence of Ca^{2+} ions triggers the precipitation of $CaCO_3$, according to Eq. 2. The precipitation mechanism of $CaCO_3$ through a carbonation route could be affected with respect to the described mechanism previously [21].

Following the described approach, this study concerns the increase of K_La and micromixing through the implementation of the packed bed reactor, since higher turbulent conditions and mass transfer rates can be achieved there than in a conventional bubbling reactor. Furthermore, the objective of this research is to study a setup that guarantees a good control over the characteristics for the $CaCO_3$ particles.

Table 5
Comparison of particle size of prepared $CaCO_3$ particles by using different reactors.

Reactor	Particle size (nm)
Rotating packed bed [4]	44–72
Tube in tube microreactor [55]	25–70
Microstructure minireactor [56]	60–110
Gas-liquid Membrane Contactor [57]	75–80 nm
surface-aerated stirred tank [58]	24–110
Gas sparged stirred tank [59]	6120
CSTR (this work)	1700–2200
PBR (this work)	220–4850

2. Materials and methods

2.1. Synthesis method

A slurry prepared with an analytical grade of CaO (Merck, purity ≥99%) and deionized water, and CO_2 (purity: 99.9%, supplied from SIAD, Italy) were employed in the synthesis of $CaCO_3$ through carbonation. Two different experimental setups were tested. The first one was a CSBR with magnetic stirring, as simple and traditional option for the synthesis through carbonation route. Then an intensified option, a PBR filled with Raschig rings as random packing, was used for this study as gas-liquid contactor.

2.1.1. Continuously stirred bubbling reactor (CSBR)

The carbonation of the CaO slurry was carried out at constant gas flowrate in a CSBR illustrated in Fig. 5a. During the synthesis, the pH and the conductivity of the suspension were monitored in order to determine when the process was concluded. The change of the pH and conductivity are related to the absorption and precipitation rate respectively through Eq. 6 and Eq. 7. The CO_2 flow was stopped once the pH was lower than 10 and the elapsed time was considered as synthesis time. In fact, according to the carbonate equilibria, below this value the CO_3^{2-} formation is not favored, thus reducing the $CaCO_3$ saturation. Then, once the process was finished, the synthesized particles were immediately filtered by vacuum (pore size = 0.45 μm) and repeatedly washed with deionized water to eliminate ion excess. At last, the $CaCO_3$ powder was dried at 60 °C overnight and it was finally ready for characterization of their size, morphology and crystal phase.

$$\left[CO_{2_{abs}}\right]\left(\frac{mol}{L}\right) = 10^{14-Initial\ pH} - 10^{14-pH} \tag{6}$$

$$\left[Ca^{2+}\right]\left(\frac{mol}{L}\right) = Conductivity\left(\frac{mS}{cm}\right) * 0.0027 + 0.0006 \tag{7}$$

Different CaO slurry concentrations and gas flowrates, between 0.015 and 0.05 mol/L and 100–1450 mL/min respectively, were tested. In such manner, it was possible to study the effect of the different operating conditions on the synthesis of $CaCO_3$. Subsequently, the mass transfer coefficient was calculated according to the correlations published by Perry [31] and Yawalkar [32], which are represented in Eq. (8) and Eq. (9) respectively:

$$K_L a = 2 * 10^{-3} * \left(\frac{P}{V_L}\right)^{0.7} * u_G^{0.5} \tag{8}$$

where, P, V_L and u_G are the stirring power (kW), liquid volume (m^3) and gas velocity (m/s)

$$K_L a = 3.35 * \left(\frac{N}{N_{cd}}\right)^{1.464} * u_G \tag{9}$$

$$N_{cd} = \frac{4 * {Q_G}^{0.5} * D^{0.25}}{T^2} \tag{10}$$

where N and N_{cd} are the stirrer speed and minimum stirrer speed for complete dispersion of the gas respectively. N_{cd} was estimated through the Eq. 10. The operating conditions, which are summarized in Table 3, were chosen in order to obtain high mass transfer coefficients between 10^{-4}–10^{-3} m/s and were calculated according to equationsEquation 8 andEquation 9 [31,32]. The values of the coefficients are in good agreement with the values obtained through CFD simulations performed by a number of researchers [33–35] and with the experimental values obtained by Alves et al. [36].

The gas residence time was determined by the ratio between the length of the reactor (0.18 m) and the terminal velocity of the bubbles generated in the sparger through the Eq. 11, Eq. 12, Eq. 13 and Eq. 14. Eq. 11 was proposed by Jamialahmad et al. [37].

$$u_{b_T} = \frac{1}{\sqrt{\frac{1}{{u_{b_{T1}}}^2} + \frac{1}{{u_{b_{T2}}}^2}}} \tag{11}$$

where u_{bT1} is the rise velocity when viscous effects are still important, while u_{bT2} is the corresponding velocity when surface tension effects are significant [37,38]. The velocity under each condition is determined by the following expressions: [39,40,41].

$$u_{b_{Tpot}} = \frac{1}{36}\frac{\Delta\rho * g * {d_b}^2}{\mu_L} \tag{12}$$

$$u_{b_{T1}} = u_{b_{Tpot}}\left[1 + 0.73667\frac{(g * d_b)^{\frac{1}{2}}}{u_{b_{Tpot}}}\right]^{1/2} \tag{13}$$

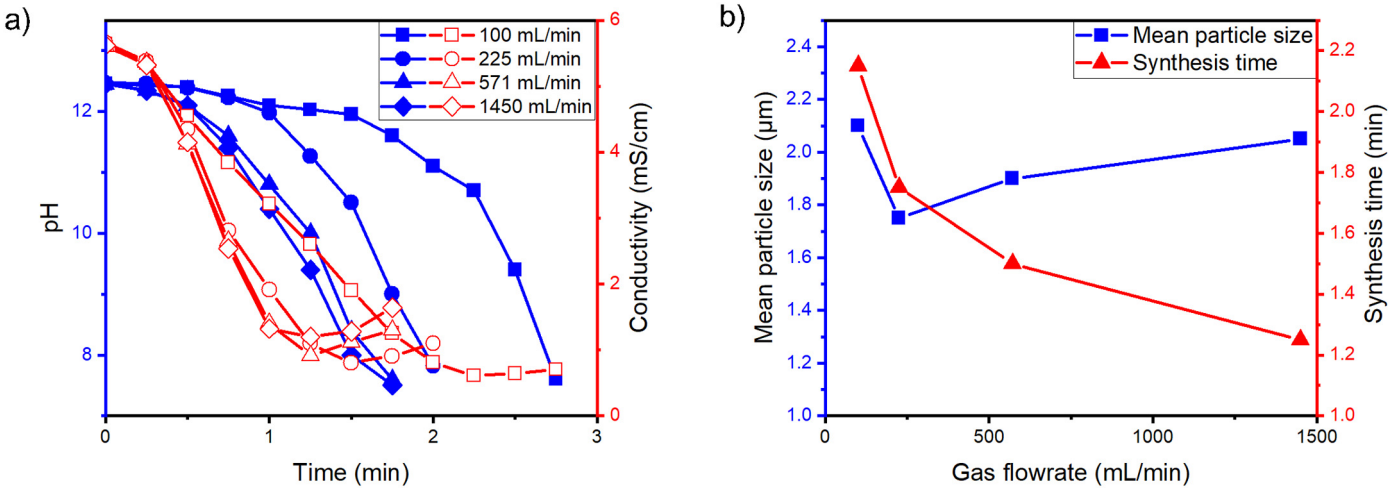


Fig. 6. Gas flowrate effect on $CaCO_3$ particles synthesis by BR alternative. a) Effect on the absorption kinetics. b) Effect on mean particle size.

$$u_{b_{T2}} = \left(\frac{3\sigma}{\rho_L d_b} + \frac{g d_b \Delta\rho}{2\rho_L}\right)^{1/2} \quad (14)$$

where $u_{b_{Tpot}}$, $\Delta\rho$, g, d_b, μ_L and ρ_L are the terminal velocity for a bubble in potential flow, density difference between the liquid and the gas, gravity acceleration, bubble size, viscosity and density of the liquid respectively.

The bubble size was estimated by a series of correlations published in [42]. According to our operating conditions ($Re_0 > 2100$ and $vol_0 > \left[\frac{20(\sigma d_0 g)^5}{(g\Delta\rho)^2\rho_L}\right]^{1/3}$, where d_0 is the hole diameter and Re_0 is the Reynolds number through the hole), the valid expression for the determination of the bubble size is reported in Eq. 15.

$$d_b = \left(\frac{72\rho_L}{\pi^2 g\Delta\rho}\right)^{1/5} Q_{G0} \quad (15)$$

2.1.2. Packed bed reactor (PBR)

In this case, the slurry is pumped through a peristaltic pump to the PBR, where it gets in contact with the CO_2 and the precipitation takes place. Specchia et al. [47] obtained higher K_La for concurrent up-flow than the obtained for concurrent down-flow determined by Reiss [48], therefore, it was decided to perform the tests in concurrent up-flow conditions. The precipitated particles are recirculated to the vessel, which is maintained at a constant stirring velocity. In such a way, two zones are individuated (See Fig. 5b): *i*) the crystallization one, inside the PBR, *ii*) the stabilization one, inside the feed tank, where the pH is high enough to provide a stable environment for the $CaCO_3$ particles, since under alkaline conditions growth and agglomeration phenomena of the CCnP are not favored [3]. In the same manner as the CSBR experiments, the synthesis time was determined once the pH reached a value less than 10 and the process was stopped. The particles were subsequently filtered and dried over night at 60 °C. The parameters of the PBR are summarized in Table 2.

In the same manner to the previous case, different CaO slurry concentrations and gas flowrates between 0.015 and 0.05 mol/L and 100–1450 mL/min respectively. In addition to those parameters, in this case, also the liquid flowrate was also varied in order to determine their effect on the synthesis of $CaCO_3$.

The different runs are summarized in Table 4, indicating the different process parameters. The residence times shown in this table were calculated from the volume of the PBR free of packaging, i.e. 29 mL. The initial CaO concentration and gas flowrates employed were selected in order to have the same initial conditions and same CO_2 consumptions to those studied in the CSBR and make valid conclusions. On the other hand, the values of the liquid flowrates were varied in order to get different mass transfer coefficients which were calculated according to correlations (see Eq. 16) published in [49,50], obtaining values higher than 10^{-2} 1/s for any considered case. This means an improvement in the mass transfer coefficient. Furthermore, the flow regime was always dispersed bubble in these conditions, according to the correlation for flow regime in a PBR published by Murugesan [30]. Consequently, segregation and polydispersity issues presented in the CSBR are expected to be reduced.

$$\ln K_L a = 73.5u_G + 32.4u_L - 3.49 \quad (16)$$

2.2. Particles characterization

Different characterization analyses were performed on the $CaCO_3$ powder. The dried powder was re-dispersed in isopropanol (0.5 g/L) and about 1 mL of sample was put into a disposable cuvette for the measurement of size and size distribution by the dynamic light scattering (DLS) method using particle size analyser (Malvern nano ZS model).

The phase purity of the samples was examined by X-Ray diffraction (Panalytical X'Pert Pro) in the 2θ range of 20–70° with a scanning step of 0.013° and a radiation CuKα, k = 1.54056 Å. The crystalline phase was identified by employing the Powder Diffraction File PDF-2 of JCPDS. The morphological characterization was obtained by using field emission scanning electron microscopy (ZEISS MERLIN FE-SEM operated at 3 kV). The samples were prepared for electron microscopy observations by suspending a small quantity of nanoparticles in isopropanol, through ultrasonic mixing for 30 min, and subsequently by placing a drop of the dispersion on a copper grid coated with a layer of amorphous carbon.

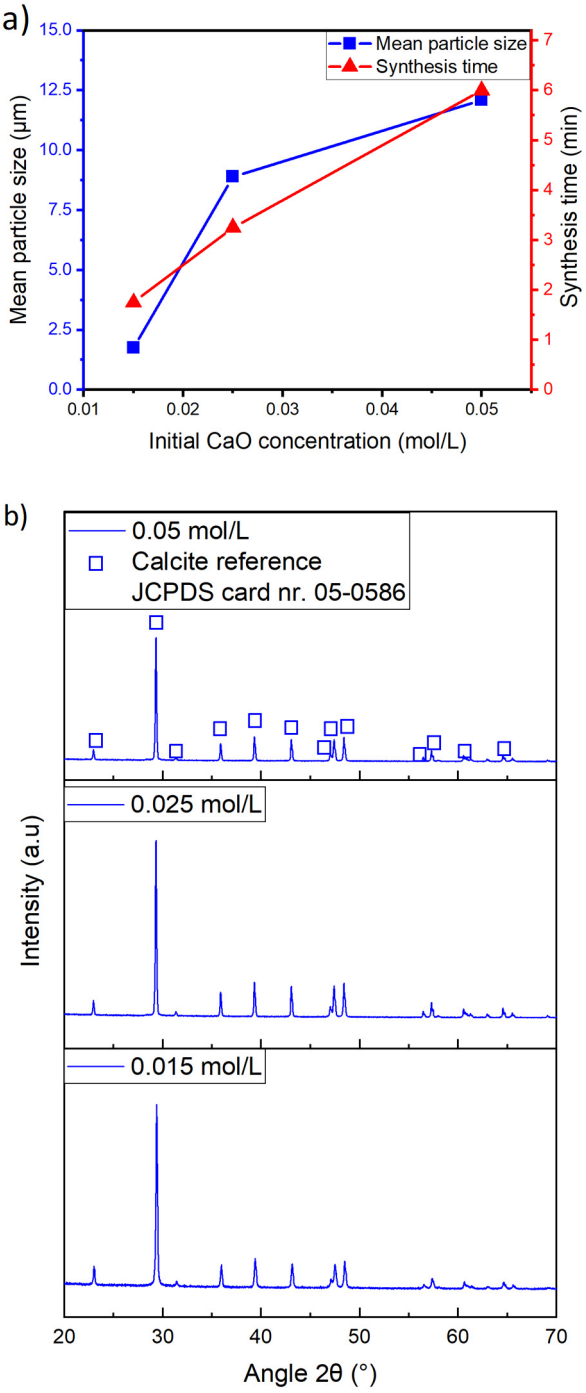


Fig. 7. Initial CaO concentration on $CaCO_3$ particles synthesis by BR alternative.

3. Results and discussion

3.1. Continuously stirred bubbling reactor (CSBR) performance

In the CSBR, the effect was explored of the initial calcium concentration and of the gas flowrate on the process and particles properties such as size, morphology and crystalline phase. The stirring velocity during this exploration, was maintained constant for every run (1200 rpm).

3.1.1. Effect of the gas flowrate

Fig. 6 shows the effect of the gas flowrate on the synthesis of the $CaCO_3$ particles. The reaction temperature, the initial CaO concentration and the stirring velocity were, 20 (±1) °C, 0.015 mol/L and 1200 rpm, respectively. At the beginning of the carbonation process the pH value underwent little variation. However, it reached an inflection point which was due to the consumption of OH^- ions, according to Eq. 4 and 5. In contrast, the conductivity decreased linearly due to the consumption of Ca^{2+} ions. The end of the synthesis was determined when the pH reached a value of less than 10, which corresponded to a minimum in the conductivity indicating that $CaCO_3$ was no longer precipitating.

The behaviour described above corresponded to the optimal one and it was obtained under the conditions of runs 1 and 2, as illustrated in Fig. 6a. In these runs, at the beginning of the process the value of the pH was high enough to provides stability to the formed particles disfavouring the agglomeration and growth phenomena [3,10]. A high rate of CO_2 absorption implies lower synthesis time and faster precipitation of the salt, and results in smaller particles obtained [4]. In fact, smaller particles were obtained for 225 mL/min (run 2) than for 100 mL/min (run 1), where a high synthesis time was obtained. Instead, for runs 3 and 4, where higher CO_2 flowrates were employed, both pH and conductivity decreased rapidly. This means that in these cases, the higher CO_2 flowrate led to a higher rate of reaction of the OH^- ions in Eq. 4 than in Eq. 5. It follows that the absorption rate is higher than the precipitation rate, since the change of the conductivity does not vary greatly with respect to the previous runs. At these pH values, the precipitated particles are not very stable and tend to agglomerate and grow [10]. Therefore, the particle size initially decreased due to the increase of the gas flowrate from 100 to 250 mL/min, but a further increase of the gas flowrate led to larger particle sizes, as shown in Fig. 6b.

3.1.2. Effect of the initial CaO concentration

By maintaining constant temperature, gas flowrate and stirring speed, equal to 20 (±1) °C, 225 mL/min and 1200 rpm respectively, the effect of the initial calcium oxide concentration on the $CaCO_3$ synthesis was studied. 0.015, 0.025 and 0.05 mol/L were tested as initial CaO concentrations. Fig. 7a shows that an increment of the initial CaO concentration brought the system towards longer synthesis times. The rate of transformation of CO_2 and HCO_3^- ions to the formation of CO_3^{2-} ions, according to Eq. 4 and Eq. 5, is enhanced by the higher concentration of OH^- ions. However, since the $CaCO_3$ precipitation rate is almost constant and it is practically independent on the calcium concentration, the synthesis time was higher by increasing the initial CaO

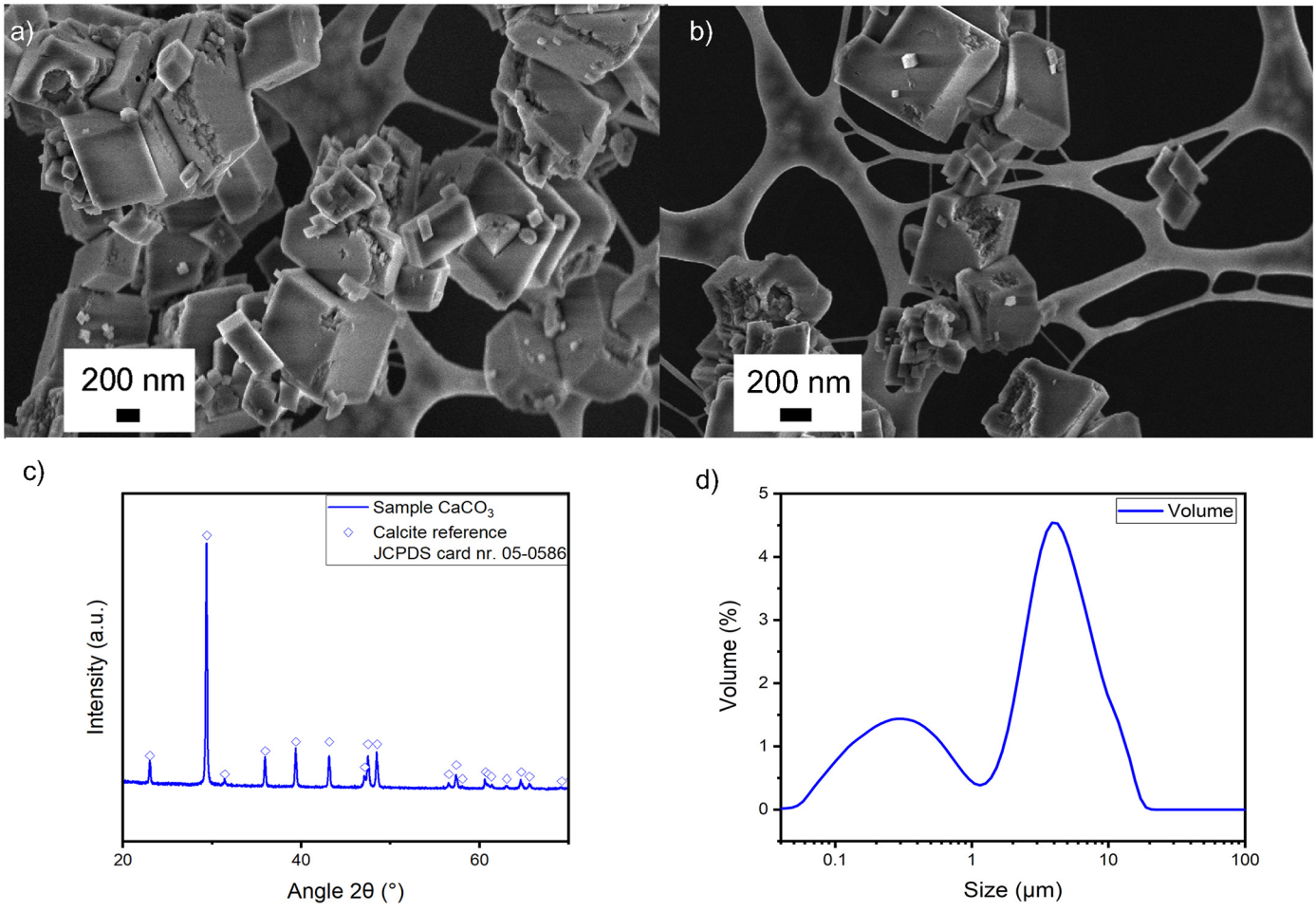


Fig. 8. $CaCO_3$ particles synthesized according to the operation parameters in run 2. (a-b) FESEM micrograph, (c) XRD spectra of $CaCO_3$ sample (Compared to calcite reference peaks extracted from PDF-2 database) and (d) PSD of the sample.

concentration. As in the previous case, longer synthesis times led to the production of larger particles.

The initial CaO concentration had no effect on the crystalline phase, as in the case of the study of the gas flowrate, just calcite was obtained for each CaO concentration according to the XRD analysis shown in Fig. 7b (calcite reference JCPDS card nr. 05–0586). This occurred because, as explained before, calcite is the most stable polymorph of $CaCO_3$ [5,20,21], and since there is no presence of extraneous ions or compounds that can stabilize other polymorph forms [5,21,23,43,44], the formation of calcite was always favored.

Consequently, the best performance of this experimental setup was obtained with the operating conditions of the run 2. Fig. 8 shows the characterization of the particles synthesized in those conditions, where the smallest cubic particles were obtained, as shown in Fig. 8a in the FESEM micrographs. This is the classical morphology of calcite, which is the only crystalline phase present, according to the XRD spectra shown in Fig. 8b. These cubic particles are present in different dimensions, being in good agreement to the laser diffraction analysis, where a wide Particle Size Distribution (PSD) was obtained, as shown in Fig. 8c. The wide distribution is probably due to agglomeration phenomena, but also to heterogeneous process due to the segregation issues present in this kind of reactor, as shown in the CFD modulations carried out by Devi et al. [35]. Larger particles and wider PSD obtained with this reactor may be due to the back-mixing and recirculation issues [45] and characteristic exponential residence time distribution of a CSTR [46]. Hence, the PSD is in good agreement to the FESEM micrograph, where cubic particles with different sizes are shown.

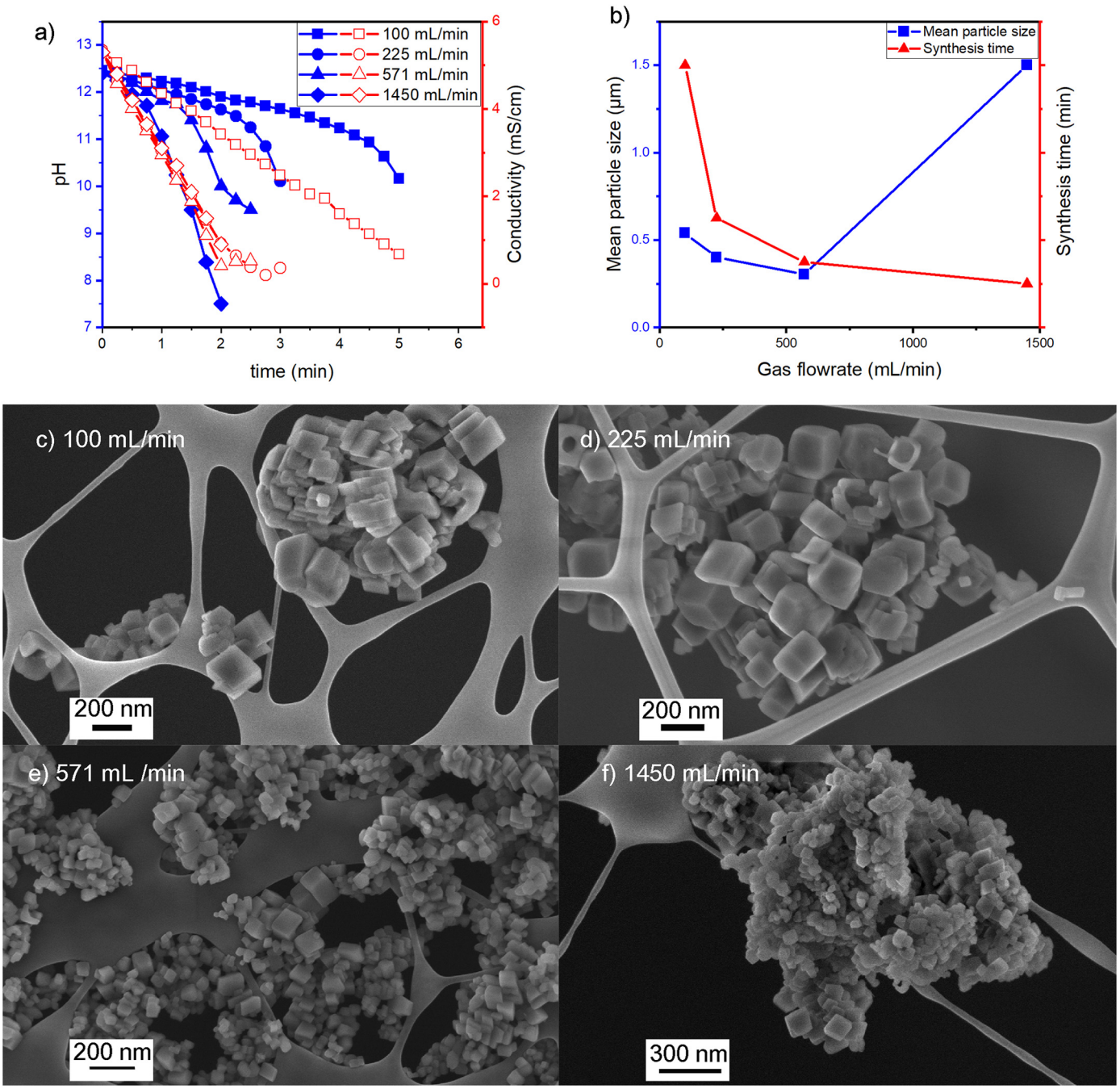


Fig. 9. Gas flowrate effect on $CaCO_3$ particles synthesis by PBR alternative. a) Effect on the absorption kinetics. b) Effect on mean particle size. c-f) Effect on morphology.

3.2. Packed bed reactor (PBR) performance

In the packed bed reactor, in addition to the study of the effect of the initial calcium concentration and the gas flowrate on the process and on the particles' properties, the effect of the liquid flowrate was also tested.

3.2.1. Effect of the gas flowrate

Fig. 9 shows the effect of the gas flowrate on the synthesis of the particles. In these tests, the reaction temperature, liquid flowrate, initial CaO and the stirring velocity were 20 (±1) °C, 108 mL/min, 0.015 mol/L and 1200 rpm, respectively. Fig. 9a shows that the reduction of the pH was faster with an increase in the gas flowrate, therefore, the rate of formation and the subsequent consumption of CO_3^{2-} ions due to $CaCO_3$ precipitation, according to Eq. 4, Eq. 5 and Eq. 2, were higher. The increase of the precipitation rate can be appreciated by the increase of the slope in the conductivity vs time curve, which indicates the consumption of the Ca^{2+} ions. Therefore, the higher final conductivity obtained by increasing the gas flowrate indicates that the conversion is lower by increasing the gas flowrate, despite the higher absorption and precipitation rates. Hence, after reaching a pH value lower than 10, the CO_3^{2-} is no longer favored, as can be seen from the plateau at the end of the reaction indicating the end of the synthesis. In such a way, the synthesis time was reduced by increasing the gas flowrate, as seen in Fig. 9b.

The mean particle size, determined by the DLS measurements and the FESEM images, is also shown in Fig. 9b. The particle size was reduced by increasing the gas flowrate, but for the highest flowrate (1450 mL/min) the DLS measurements indicated microsized particles

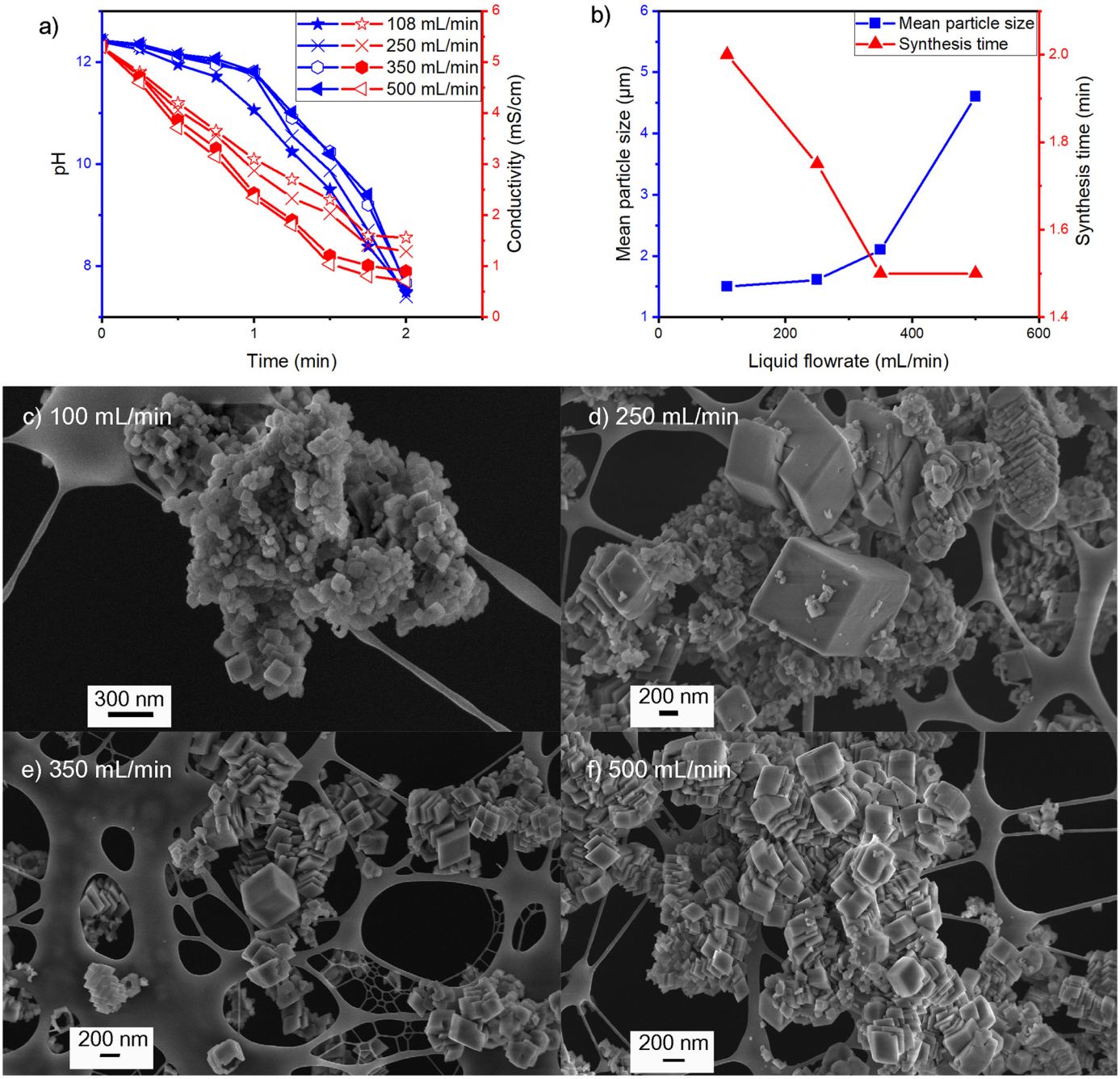


Fig. 10. Liquid flowrate effect on CaCO3 particles synthesis by PBR alternative. a) Effect on the absorption kinetics. b) Effect on mean particle size. c-f) Effect on morphology.

(1.5 μm). This value corresponds to the size of the aggregated primary nanoparticles as seen in the corresponding FESEM micrograph. The formation of these aggregates was probably due to the fast pH reduction and consequently instability of $CaCO_3$ particle [3,10]. In all cases, cubic calcite particles were obtained, i.e. the gas flowrate had no effect on the polymorphism of the particles.

3.2.2. Effect of the liquid flowrate

The effect of the liquid flowrate on the $CaCO_3$ synthesis was studied by maintaining constant the following operating parameters: temperature, gas flowrate, initial CaO concentration and stirring speed, equal to 20 (±1) °C, 225 mL/min, 0.015 mol/L and 1200 rpm respectively. In this case, increasing liquid flowrates maintained a high pH during the synthesis, as shown in Fig. 10a. Higher flowrates led to higher precipitation rates and calcium conversions according to the conductivity vs time curve. Anyway, a different precipitation mechanism can be supposed, since at higher liquid flowrates both cubic and laminated cubic particles were present, as seen in Fig. 10b. In fact, the presence of laminated cubic particles was more evident by increasing the liquid flowrates. This was probably due to that micromixing was surely affected; and growth phenomena was favored over nucleation.

3.2.3. Effect of the initial CaO concentration

The effect of the initial calcium oxide concentration on the $CaCO_3$ synthesis was studied by maintaining temperature, gas, liquid flowrate and stirring speed as constant, equal to 20 (±1) °C, 225 mL/min, 108 mL/min and 1200 rpm respectively. Three different concentrations were studied, specifically 0.015, 0.025 and 0.05 mol/L. Fig. 11a shows that, as for CSBR, an increment of the initial CaO concentration led to longer synthesis times and larger particles. The initial CaO concentration had no effect on the crystalline phase, similar to the case of CSBR, and pure calcite was obtained for each CaO concentration, as shown in Fig. 11b (calcite reference JCPDS card nr. 05–0586).

Therefore, the conditions corresponding to run 9 (see Table 4) were determined as optimal conditions and the characterization of these particles is presented in Fig. 12. PSD shows nanosized particles with a mean particle size equal to 300 nm, which is not in good agreement to the FESEM micrographs, where cubic primary calcite particles with sizes between 40 and 200 nm are shown. This is probably because the DLS measurements consider the size of the formed agglomerates and not the primary particles one. On the other hand, the cubic particles (classical morphology of calcite) shown by the FESEM micrographs are in good agreement to the XRD spectra, where pure calcite as crystalline phase was determined.

3.3. Reactors comparison

The performance of both reactors was studied and compared by varying the gas flowrate and maintaining constant the temperature, concentration of CaO, stirring velocity and liquid flowrate in the case of the PBR equal to 20 (±1) °C, 0.015 mol/L, 1200 rpm and 225 mL/min, respectively. By employing the PBR, the synthesis of $CaCO_3$ through carbonation method was improved with respect to the CSBR performance. Fig. 13a shows that there was an intensification regarding the mean particle size, since an enhancement from synthesizing micro and polydispersed particles to produce dispersed nanosized cubic calcite particles was observed. This can be associated to the higher mass transfer coefficients provided by the PBR and, consequently, micromixing shorter times. Shorter micromixing times mean higher nucleation rates over growth [4,51,52]. Micromixing has an important effect on the particle size distribution, since a poor micromixing leads to highly nonlinear nucleation and growth kinetics of crystals. If micromixing time is too high, the nucleation and growth of crystals had already begun before micromixing in the precipitator was complete. As a consequence, the poor micromixing present in the CSBR led to supersaturation gradients present in the nonhomogeneous mixture, which result in a wider PSD [51,53,54]. Furthermore, higher conversions of calcium and CO_2 were reached by employing the PBR, as seen in Fig. 13b. The higher mass transfer coefficients reached with this kind of setup led to a more sustainable precipitation process.

Moreover, the PBR provides a better control over the particle size and morphology compared to the CSTR, in which only microsized particles can be obtained. In the literature, some different reaction setups have been proposed for the synthesis particles of $CaCO_3$, which are devoted to the production of either nano or micro particles, as shown in Table 5, with limited possibility of tailoring the particle size outside design ranges. Instead, the original PBR setup allows to easily obtain a wider set of dimensions by varying some operating parameters with

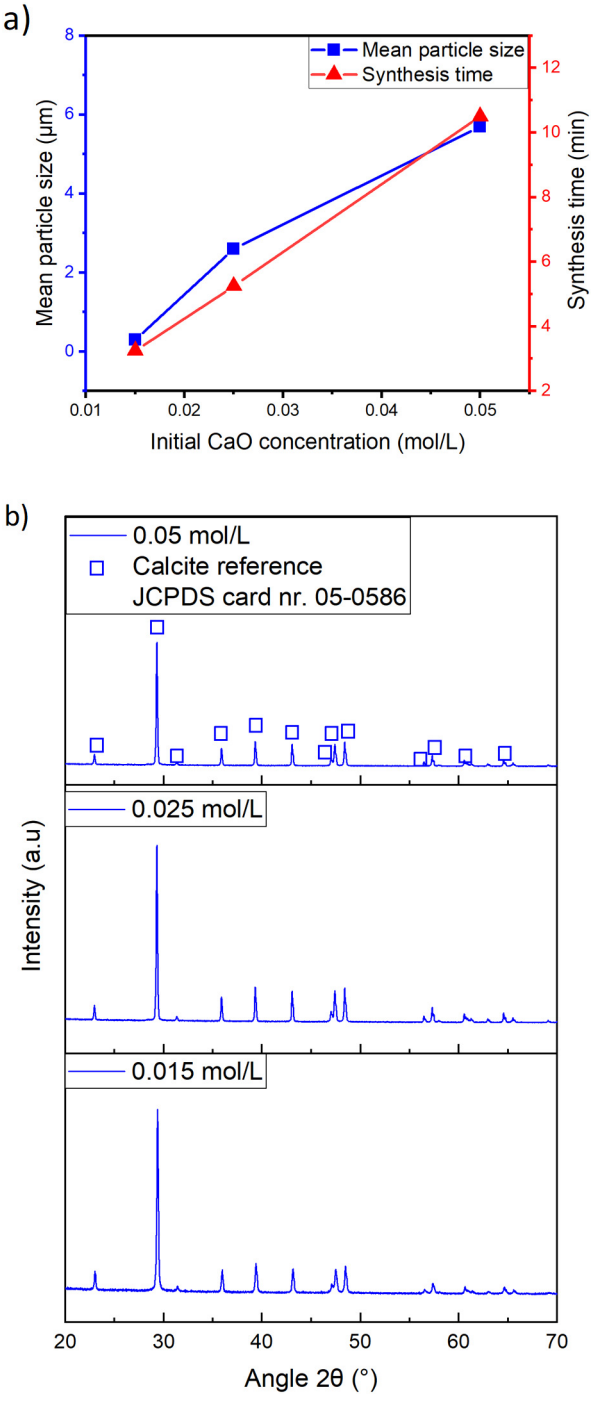


Fig. 11. Initial CaO concentration on CaCO3 particles synthesis by PBR alternative.

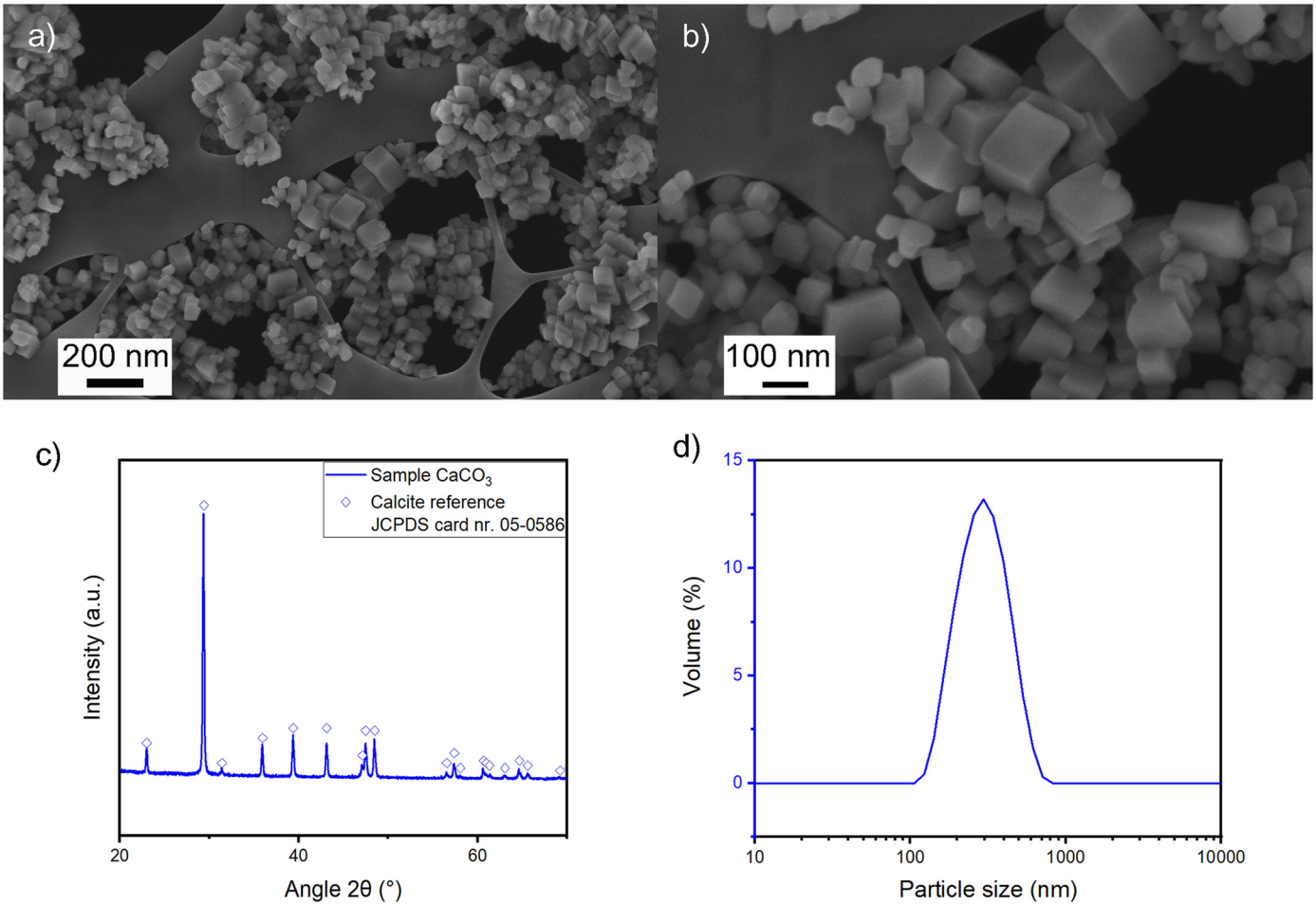


Fig. 12. $CaCO_3$ particles synthesized according to the operation parameters in run 9. (a-b) FESEM micrograph, (c) XRD spectra of $CaCO_3$ sample (Compared to calcite reference peaks extracted from PDF-2 database) and (d) PSD of the sample.

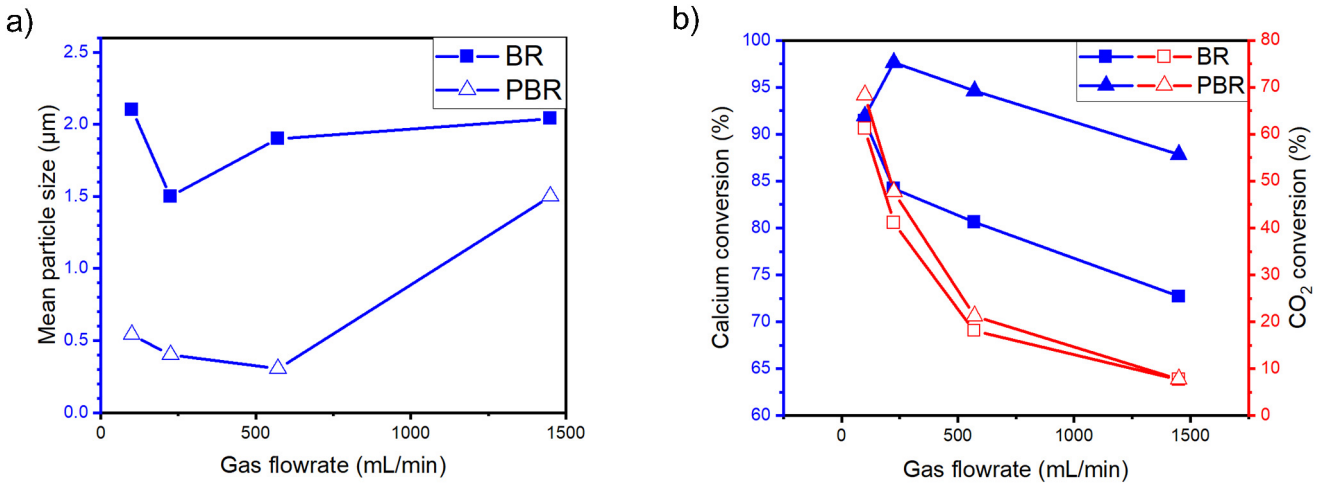


Fig. 13. Reactors performance comparison. a) Mean particle size by varying the gas flowrate. b) Calcium and CO_2 conversions on both alternatives, CSBR and PBR.

the aim of targeting specific particle size distributions. Furthermore, the PBR also avoids high energy consumptions and high pressure drops, which can be observed in other synthesis apparatus as rotating packed beds, microreactors or membrane contactors requiring high electrical power and gas pressure respectively.

4. Conclusions

An intensification process was carried out, by employing a packed bed reactor (PBR) setup to produce $CaCO_3$ nanoparticles through the carbonation route. The properties of the $CaCO_3$ are easily tuneable by

varying the operating parameters of the PBR, therefore particles with different characteristics can be obtained for a wide field of applications. The preliminary issues presented by a continuously stirred bubbling reactor (CSBR) were reduced by maximizing the effectiveness of intra-and intermolecular events, i.e. enhancing the macro and micromixing. Thus, the same processing experience was given to each molecule in order to obtain a product with uniform properties. Microsized particles with a wide PSD were synthesized with the BR. While, the PBR provided growth and agglomeration control at optimum conditions that led to synthesizing of nanosized particles with a narrow PSD. In this way, the conventional process was enhanced in an intensified process, where nanosized calcite cubic particles were synthesized with an increase in process conversions in terms of calcium and CO_2.

Declaration of Competing Interest

The authors declare that they have no known competing financial interests or personal relationships that could have appeared to influence the work reported in this paper.

Acknowledgements

This project has received funding from the European Union's Horizon 2020 Research and Innovation Programme under Grant Agreement No. 768583. This paper reflects only the author's view and the content is the sole responsibility of the authors. The European Commission or its services cannot be held responsible for any use that may be made of the information it contains.

References

[1] L. Rodgers, No Title, Clim. Chang. Massive CO2 Emit. You May Not Know About, https://www.bbc.com/news/science-environment-46455844 2018.
[2] E.I. Koytsoumpa, C. Bergins, E. Kakaras, The CO2 economy: review of CO2 capture and reuse technologies, J. Supercrit. Fluids 132 (2018) 3–16, https://doi.org/10.1016/J.SUPFLU.2017.07.029.
[3] E. Ulkeryildiz, S. Kilic, E. Ozdemir, Nano-CaCO 3 synthesis by jet flow, Colloids Surfaces A Physicochem. Eng. Asp. 512 (2017) 34–40, https://doi.org/10.1016/j.colsurfa.2016.10.037.
[4] B. Sun, X. Wang, J. Chen, G. Chu, J. Chen, L. Shao, Synthesis of nano-CaCO 3 by simultaneous absorption of CO 2 and NH 3 into CaCl 2 solution in a rotating packed bed, Chemical Eng Journal 168 (2011) 731–736, https://doi.org/10.1016/j.cej.2011.01.068.
[5] A. Declet, E. Reyes, O.M. Suárez, Calcium carbonate precipitation: a review of the carbonate crystallization process and applications in bioinspired composites, Rev. Adv. Mater. Sci. 44 (2016) 87–107.
[6] C. Ramakrishna, T. Thenepalli, J.W. Ahn, Evaluation of various synthesis methods for calcite-precipitated calcium carbonate (PCC) formation, Korean Chem. Eng. Res. 55 (2017) 279–286, https://doi.org/10.9713/kcer.2017.55.3.279.
[7] M.Y. RYU, K.S. YOU, J.W. AHN, H. KIM, Effect of the pH and basic additives on the precipitation of calcium carbonate during carbonation reaction, Resour. Process. 54 (2009) 14–18, https://doi.org/10.4144/rpsj.54.14.
[8] Y. Wen, L. Xiang, Y. Jin, Synthesis of plate-like calcium carbonate via carbonation route, Mater. Lett. (2003) https://doi.org/10.1016/S0167-577X(02)01312-5.
[9] J. Rieger, M. Kellermeier, L. Nicoleau, Formation of nanoparticles and nanostructures-an industrial perspective on CaCO3, cement, and polymers, Angew. Chemie - Int. Ed. 53 (2014) 12380–12396, https://doi.org/10.1002/anie.201402890.
[10] S. Kilic, G. Toprak, E. Ozdemir, Stability of CaCO3 in ca(OH)2 solution, Int. J. Miner. Process. (2016) https://doi.org/10.1016/j.minpro.2015.12.006.
[11] X. Liu, L. Chen, A. Liu, X. Wang, Effect of nano-CaCO3 on properties of cement paste, Energy Procedia 16 (2012) 991–996, https://doi.org/10.1016/j.egypro.2012.01.158.
[12] I. Cosentino, L. Restuccia, G.A. Ferro, F. Liendo, F. Deorsola, S. Bensaid, Evaluation of the mechanical properties of cements with fillers derived from the CO2 reduction of cement plants, Procedia Struct. Integr. 18 (2019) 472–483, https://doi.org/10.1016/J.PROSTR.2019.08.189.
[13] C. Maier, T. Calafut, C. Maier, T. Calafut, Fillers and reinforcements, Polypropylene (1998) 49–56, https://doi.org/10.1016/B978-188420758-7.50009-6.
[14] R. Ragipani, S. Bhattacharya, A.K. Suresh, Towards efficient calcium extraction from steel slag and carbon dioxide utilisation via pressure-swing mineral carbonation, React. Chem. Eng. 4 (2019) 52–66, https://doi.org/10.1039/c8re00167g.
[15] S. Tinchana, J. Chungsiriporn, C. Bunyakan, Leaching of Steelmaking Slag using Acetic Acid Solution and Deionized Water for CO 2 Sequestration, 2012 45–48.
[16] R.S. Somani, K.S. Patel, A.R. Mehta, R.V. Jasra, Examination of the polymorphs and particle size of calcium carbonate precipitated using still effluent (i.e., CaCl2 + NaCl solution) of soda ash manufacturing process, Ind. Eng. Chem. Res. 45 (2006) 5223–5230, https://doi.org/10.1021/ie0513447.
[17] A. Lin, M.A. Meyers, Growth and structure in abalone shell, Mater. Sci. Eng. A (2005) https://doi.org/10.1016/j.msea.2004.06.072.
[18] H. Ghaedamini, M.C. Amiri, Effects of temperature and surfactant concentration on the structure and morphology of calcium carbonate nanoparticles synthesized in a colloidal gas aphrons system, J. Mol. Liq. (2019) https://doi.org/10.1016/j.molliq.2019.02.119.
[19] K. Sawada, The mechanisms of crystallization and transformation of calcium carbonates, Pure Appl. Chem. 69 (2007) 921–928, https://doi.org/10.1351/pac199769050921.
[20] J. Kawano, N. Shimobayashi, A. Miyake, M. Kitamura, Precipitation diagram of calcium carbonate polymorphs: Its construction and significance, J. Phys. Condens. Matter. 21 (2009) https://doi.org/10.1088/0953-8984/21/42/425102.
[21] C.R. Blue, A. Giuffre, S. Mergelsberg, N. Han, J.J. De Yoreo, P.M. Dove, Chemical and physical controls on the transformation of amorphous calcium carbonate into crystalline CaCO3 polymorphs, Geochim. Cosmochim. Acta (2017) https://doi.org/10.1016/j.gca.2016.09.004.
[22] Z. Amjad, R.W. Zuhl, Calcium carbonate precipitation in the presence of inhibitors, Mater. Perform. 46 (2007) 42–47.
[23] Y. Boyjoo, V.K. Pareek, J. Liu, Synthesis of micro and nano-sized calcium carbonate particles and their applications, J. Mater. Chem. A 2 (2014) 14270–14288, https://doi.org/10.1039/c4ta02070g.
[24] J. Chen, L. Shao, Mass production of nanoparticles by high gravity reactive precipitation technology with low cost, China Particuology (2007) https://doi.org/10.1016/s1672-2515(07)60110-9.
[25] A. Tamir, Y. Taitel, The effect of the gas side resistance on absorption with chemical reaction from binary mixtures, Chem. Eng. Sci. (1975) https://doi.org/10.1016/0009-2509(75)85025-1.
[26] H. Zhao, L. Shao, J.F. Chen, High-gravity process intensification technology and application, Chem. Eng. J. 156 (2010) 588–593, https://doi.org/10.1016/j.cej.2009.04.053.
[27] A. Ataki, H.J. Bart, The use of the VOF-model to study the wetting of solid surfaces, Chem. Eng. Technol. 27 (2004) 1109–1114, https://doi.org/10.1002/ceat.200402091.
[28] A. Ataki, H.J. Bart, Experimental and CFD simulation study for the wetting of a structured packing element with liquids, Chem. Eng. Technol. 29 (2006) 336–347, https://doi.org/10.1002/ceat.200500302.
[29] L. Zhao, R.L. Cerro, Experimental characterization of viscous film flows over complex surfaces, Int. J. Multiph. Flow. (1992) https://doi.org/10.1016/0301-9322(92)90048-L.
[30] T. Murugesan, V. Sivakumar, Pressure drop and flow regimes in cocurrent gas-liquid upflow through packed beds, Chem. Eng. J. (2002) https://doi.org/10.1016/S1385-8947(02)00039-6.
[31] R. Perry, S. Perry, D. Green, J. Maloney, Perry's Chemical Engineers' Handbook, 7th ed., 1997 https://doi.org/10.1021/ed027p533.1.
[32] A.A. Yawalkar, A.B.M. Heesink, G.F. Versteeg, V.G. Pangarkar, Gas-liquid mass transfer coefficient in stirred tank reactors, Can. J. Chem. Eng. 80 (2008) 840–848, https://doi.org/10.1002/cjce.5450800507.
[33] P. Ranganathan, S. Sivaraman, Investigations on hydrodynamics and mass transfer in gas-liquid stirred reactor using computational fluid dynamics, Chem. Eng. Sci. (2011) https://doi.org/10.1016/j.ces.2011.03.007.
[34] T. Moucha, V. Linek, K. Erokhin, J.F. Rejl, M. Fujasová, Improved power and mass transfer correlations for design and scale-up of multi-impeller gas-liquid contactors, Chem. Eng. Sci. 64 (2009) 598–604, https://doi.org/10.1016/j.ces.2008.10.043.
[35] T.T. Devi, B. Kumar, Mass transfer and power characteristics of stirred tank with Rushton and curved blade impeller, Eng. Sci. Technol. an Int. J. 20 (2017) 730–737, https://doi.org/10.1016/j.jestch.2016.11.005.
[36] S. Alves, C. Maia, J.M. Vasconcelos, Experimental and modelling study of gas dispersion in a double turbine stirred tank, Chem. Eng. Sci. 57 (2002) 487–496, https://doi.org/10.1016/S0009-2509(01)00400-6.
[37] M. Jamialahmadi, C. Branch, H. Muller steinhagen, Terminal bubble rise velocity in liquids, Chem. Eng. Res. Des. 72 (1994) 119–122. https://www.cheric.org/research/tech/periodicals/view.php?seq=51476.
[38] S. Baz-Rodríguez, A. Aguilar-Corona, A. Soria, Rising velocity for single bubbles in pure liquids, Rev. Mex. Ing. Quim. 11 (2012) 269–278.
[39] V.G. Levich, Physicochemical Hydrodynamics, Prentice-Hall, Englewood Cliffs, N.J, 1962.
[40] D.W. Moore, The boundary layer on a spherical gas bubble, J. Fluid Mech. 16 (1963) 161–176, https://doi.org/10.1017/S0022112063000665.
[41] I.H. Lehrer, A rational terminal velocity equation for bubbles and drops at intermediate and high Reynolds numbers, J. Chem. Eng. Japan. 9 (1976) 237–240, https://doi.org/10.1252/jcej.9.237.
[42] R.E. Treybal, Mass-transfer operations, 2nd ed. McGraw-Hill Book Company, Inc, New York, 1955 1956, https://doi.org/10.1002/aic.690020430.
[43] B. Njegić-Džakula, G. Falini, L. Brečević, Ž. Skoko, D. Kralj, Effects of initial supersaturation on spontaneous precipitation of calcium carbonate in the presence of charged poly-l-amino acids, J. Colloid Interface Sci. 343 (2010) 553–563, https://doi.org/10.1016/J.JCIS.2009.12.010.
[44] Q. Hu, J. Zhang, H. Teng, U. Becker, Growth process and crystallographic properties of ammonia-induced vaterite, Am. Mineral. 97 (2012) 1437–1445, https://doi.org/10.2138/am.2012.3983.
[45] W.H. Khan, V.K. Rathod, Process intensification approach for preparation of curcumin nanoparticles via solvent–nonsolvent nanoprecipitation using spinning disc reactor, Chem. Eng. Process. Process Intensif. 80 (2014) 1–10, https://doi.org/10.1016/J.CEP.2014.03.011.

[46] D.A. Paquet Jr., W.H. Ray, Tubular reactors for emulsion polymerization: I. Experimental investigation, AIChE J. 40 (1994) 73–87, https://doi.org/10.1002/aic.690400110.
[47] V. Specchia, S. Sicardi, A. Gianetto, Absorption in packed towers with concurrent upward flow, AIChE J. 20 (1974) 646–653, https://doi.org/10.1002/aic.690200403.
[48] L.P. Reiss, Cocurrent gas-liquid contacting in packed columns, Ind. Eng. Chem. Process. Des. Dev. 6 (1967) 486–499, https://doi.org/10.1021/i260024a017.
[49] B.F. Alexander, Y.T. Shah, Gas-liquid mass transfer coefficients for cocurrent upflow in packed beds — effect of packing shape at low flow rates, Can. J. Chem. Eng. 54 (1976) 556–559, https://doi.org/10.1002/cjce.5450540613.
[50] K.M. Takahashi, R.C. Alkire, Mass transfer from dispersed bubbles to electrolyte solution in packed beds, AIChE J. 34 (1988) 1504–1510, https://doi.org/10.1002/aic.690340912.
[51] J. Chen, C. Zheng, Gant Ang Chen, interaction of macro- and micromixing on particle size distribution in reactive precipitation, Chem. Eng. Sci. 51 (1996) 1957–1966, https://doi.org/10.1016/0009-2509(96)00053-X.
[52] N.S. Tavare, Mixing, reaction, and precipitation: interaction by exchange with mean micromixing models, AICHE J. 41 (1995) 2537–2548, https://doi.org/10.1002/aic.690411204.
[53] R. Phillips, S. Rohani, J. Baldyga, Micromixing in a single-feed semi-batch precipitation process, AICHE J. 45 (1999) 82–92, https://doi.org/10.1002/aic.690450108.
[54] A.J. Mahajan, D.J. Kirwan, Micromixing effects in a two-impinging-jets precipitator, AICHE J. 42 (1996) 1801–1814, https://doi.org/10.1002/aic.690420702.
[55] Y. Liang, G. Chu, J. Wang, Y. Huang, J. Chen, B. Sun, L. Shao, Controllable preparation of nano-CaCO3 in a microporous tube-in-tube microchannel reactor, Chem. Eng. Process. Process Intensif. 79 (2014) 34–39, https://doi.org/10.1016/j.cep.2014.03.006.
[56] K. Wang, Y.J. Wang, G.G. Chen, G.S. Luo, J.D. Wang, Enhancement of mixing and mass transfer performance with a microstructure minireactor for controllable preparation of CaCO3 nanoparticles, Ind. Eng. Chem. Res. 46 (2007) 6092–6098, https://doi.org/10.1021/ie061502+.
[57] Z. Jia, Q. Chang, J. Qin, A. Mamat, Preparation of calcium carbonate nanoparticles with a continuous gas-liquid membrane contactor: particles morphology and membrane fouling, Chinese J. Chem. Eng. 21 (2013) 121–126, https://doi.org/10.1016/S1004-9541(13)60449-8.
[58] L. Ding, B. Wu, P. Luo, Preparation of CaCO3 nanoparticles in a surface-aerated tank stirred by a long-short blades agitator, Powder Technol. 333 (2018) 339–346, https://doi.org/10.1016/j.powtec.2018.04.057.
[59] J. García Carmona, J. Gómez Morales, R. Rodríguez Clemente, Rhombohedral-scalenohedral calcite transition produced by adjusting the solution electrical conductivity in the system ca(OH)2-CO2-H2O, J. Colloid Interface Sci. 261 (2003) 434–440, https://doi.org/10.1016/S0021-9797(03)00149-8.